CrossMark

J. Fluid Mech. (2015), *vol.* 772, *pp.* 630–648. © Cambridge University Press 2015
doi:10.1017/jfm.2015.223

The diameters and velocities of the droplets ejected after splashing

Guillaume Riboux[1] **and José Manuel Gordillo**[1,†]

[1]Área de Mecánica de Fluidos, Departamento de Ingeniería Aeroespacial y Mecánica de Fluidos, Universidad de Sevilla, Avenida de los Descubrimientos s/n 41092, Sevilla, Spain

(Received 2 December 2014; revised 7 April 2015; accepted 13 April 2015; first published online 7 May 2015)

When a drop impacts a smooth, dry surface at a velocity above the so-called critical speed for drop splashing, the initial liquid volume loses its integrity, fragmenting into tiny droplets that are violently ejected radially outwards. Here, we make use of the model of Riboux & Gordillo (*Phys. Rev. Lett.*, vol. 113, 2014, 024507), together with a one-dimensional approximation describing the flow in the ejected liquid sheet and of balances of mass and momentum at the border of the sheet, to calculate mean sizes and velocities of the ejected drops. The predictions of the model are in good agreement with experiments.

Key words: aerosols/atomization, breakup/coalescence, drops

1. Introduction

By the end of the nineteenth century and making use of high-speed photography, Worthington (1908) pioneered the phenomenological description of very fast hydrodynamic events, such as those caused by the impact of a drop on a solid, which take place, quoting Worthington, 'in the twinkle of an eye'. Recently, helped by advances in high-speed video imaging, many scientific papers have revealed unforeseen aspects of drop impact, among which one could cite the critical roles played by the structure of the solid surface (Richard, Clanet & Quere 2002; Duez *et al.* 2007; Bird *et al.* 2013) and by the gaseous atmosphere in promoting or inhibiting the splash (Xu, Zhang & Nagel 2005; Mandre, Mani & Brenner 2009; Duchemin & Josserand 2011; Latka *et al.* 2012). Over the past few decades, much research has been devoted to deducing a criterion for determining the precise conditions under which a drop hitting a solid surface either conserves its integrity after impact or disintegrates into smaller fragments; see Mundo, Sommerfeld & Tropea (1995), Rioboo, Marengo & Tropea (2002), Josserand & Zaleski (2003), Xu *et al.* (2005), Yarin (2006), Bird, Tsai & Stone (2009), Mandre *et al.* (2009), Driscoll, Stevens & Nagel (2010), Duchemin & Josserand (2011), Kolinski *et al.* (2012), Latka *et al.* (2012) and Palacios *et al.* (2013). However, to our knowledge, the only splash criterion that is compatible with all the available experimental evidence and which predicts the splash threshold velocity with small relative error for smooth dry surfaces is the one derived only recently by Riboux & Gordillo (2014). The theory proposed, which is supported by a

† Email address for correspondence: jgordill@us.es

https://doi.org/10.1017/jfm.2015.223 Published online by Cambridge University Press

	ρ (kg m^{-3})	σ (mN m^{-1})	μ (cP)	R (mm)	ℓ_σ (mm)	V^* (m s^{-1})	$Oh \times 10^3$
(*a*)	789	22.6	1.0	1.04	1.71	2.19	7.3
(*b*)	854	17.2	1.3	0.86	1.43	1.70	11.4
(*c*)	913	18.6	4.6	0.89	1.44	1.69	37.1
(*d*)	1000	19.5	10.0	0.90	1.41	2.01	75.3

TABLE 1. Physical properties of the different fluids used: (*a*) ethanol, (*b*) decamethyltetrasiloxane, (*c*) poly(dimethylsiloxane) and (*d*) 10 cP silicone oil. The columns show the fluid density ρ, interfacial tension coefficient σ, viscosity μ, drop radius R, capillary length ℓ_σ, impact velocity V^* for splashing and the corresponding Ohnesorge number, defined here as $Oh = \sqrt{We}/Re = \mu/\sqrt{\rho R\sigma}$.

thorough experimental study as well as by the data published in Mundo *et al.* (1995), Xu *et al.* (2005), Palacios *et al.* (2013) and Stevens (2014), shows that the critical impact velocity above which splashing occurs is reached when the extremely thin and fast liquid sheet, which is expelled in the direction tangential to the solid as a result of the impact, is accelerated vertically up to velocities greater than those caused by the capillary retraction of the liquid rim. The vertical accelerations imparted to the edge of the spreading sheet, which has a characteristic thickness of the order of a hundredth of the drop radius, are produced by the lift force exerted by the surrounding gaseous atmosphere. The lift results from the addition of the lubrication force between the lamella and the substrate, which depends strongly on the mean free path between gas molecules and on the aerodynamic forces acting at the top part of the lamella (Riboux & Gordillo 2014).

In this work we extend the theoretical results in Riboux & Gordillo (2014), from now on abbreviated R&G, to give a detailed analysis of the disintegration of the drop into tiny droplets that takes place when the impact velocity is above the critical velocity. More precisely, the goal of the present study is to express the velocities and radii of the droplets ejected after the violent impact on the solid as functions of the liquid and gas physical properties, the initial drop radius and the impact velocity.

The paper is structured as follows: in § 2 we present the phenomenological observations associated with the atomization of the splashing drop right after the impact; § 3 is dedicated to developing a theoretical model, which is validated by comparison with the experimental evidence in § 4; and § 5 summarizes the conclusions.

2. Experimental study

Experiments are performed using the same set-up as in R&G, where spherical millimetric drops of radii R fall under the action of gravity onto a dry glass slide which is partially wetted by the liquids whose physical properties are shown in table 1; the contact angle in all cases considered is close to 20°, and from now on $\nu = \mu/\rho$ will denote the liquid kinematic viscosity. The velocity V of the drops at the instant of impact is controlled by varying the vertical distance between the exit of the needles and the substrate. The impact process is recorded with two high-speed cameras, placed perpendicular to each other and operated using two different optical magnifications and acquisition speeds (see R&G and appendix A for details). Water is not included as one of the working fluids in our experimental study, because the limitations in the spatial and temporal resolutions of our high-speed cameras impede

https://doi.org/10.1017/jfm.2015.223 Published online by Cambridge University Press

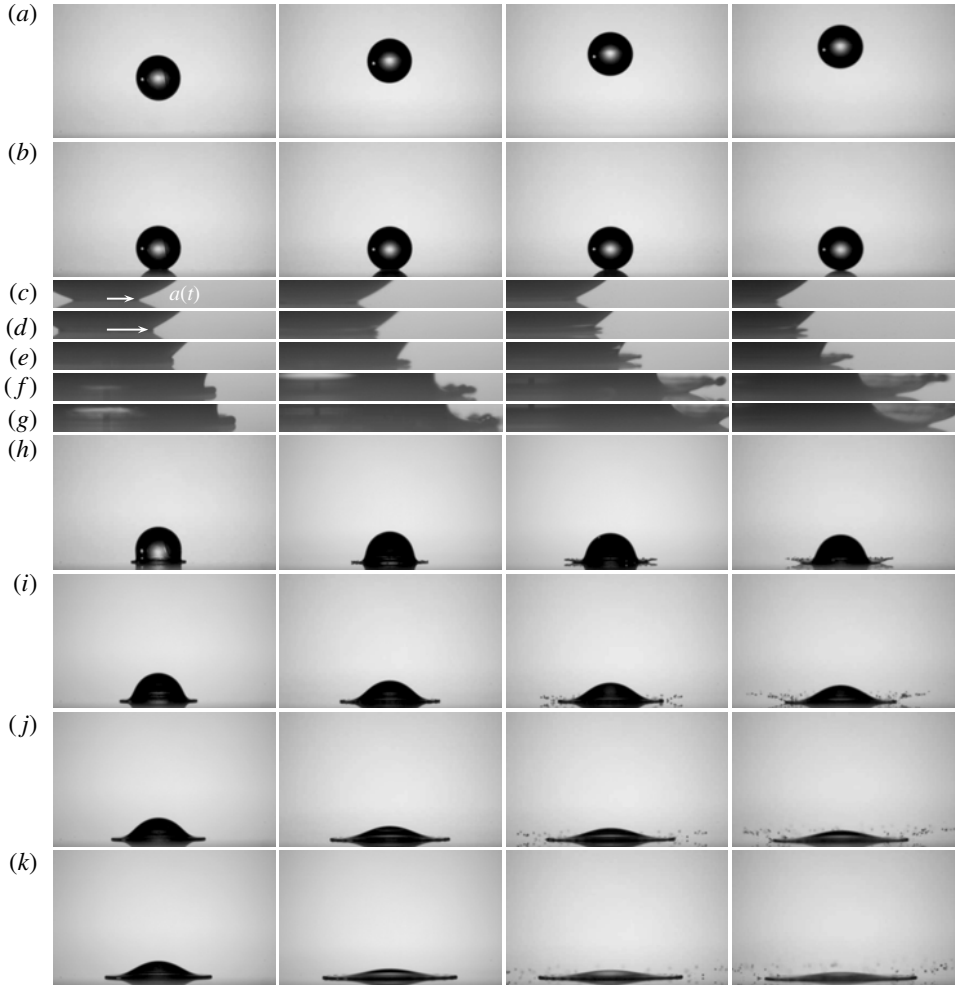

FIGURE 1. Effect of increasing impact velocity on the splashing of the drop: from left to right, the impact velocity V is 1.28 m s^{-1} (first column), 2.01 m s^{-1} (second column), 2.28 m s^{-1} (third column) and 2.58 m s^{-1} (fourth column). From top to bottom, each sequence of images corresponds to the instants when T is (*a*) -1.131 ms, (*b*) 0.029 ms, (*c*) 0.03 ms, (*d*) 0.05 ms, (*e*) 0.09 ms, (*f*) 0.21 ms, (*g*) 0.28 ms, (*h*) 0.319 ms, (*i*) 0.609 ms, (*j*) 0.899 ms and (*k*) 1.189 ms. Images (*c–g*) have a higher spatiotemporal resolution than the other images in the same column. The temporal resolutions of the high-speed cameras are 10 μs and 58 μs. The liquid is ethanol and the radius of the drop is $R = 1.04$ mm. The critical velocity for splashing is $V^* = 2.19$ m s^{-1}.

accurate measurement of the tiny sizes (just a few microns) and large velocities ($\sim$20 m s^{-1}) of the fragments ejected. Nonetheless, in appendix B we will make use of the experimental results on splashing water droplets provided in Thoroddsen, Takehara & Etoh (2012) to give further support to our theory.

Figure 1 shows the time sequence of events occurring right after a drop of a liquid with viscosity $\mu = 1$ cP falls onto the solid at increasing impact velocities. For the smallest value of V (figure 1, first column), a liquid sheet of thickness $H_t \ll R$ is expelled radially outwards and tangentially to the wall with a velocity $V_t \gg V$ for

https://doi.org/10.1017/jfm.2015.223 Published online by Cambridge University Press

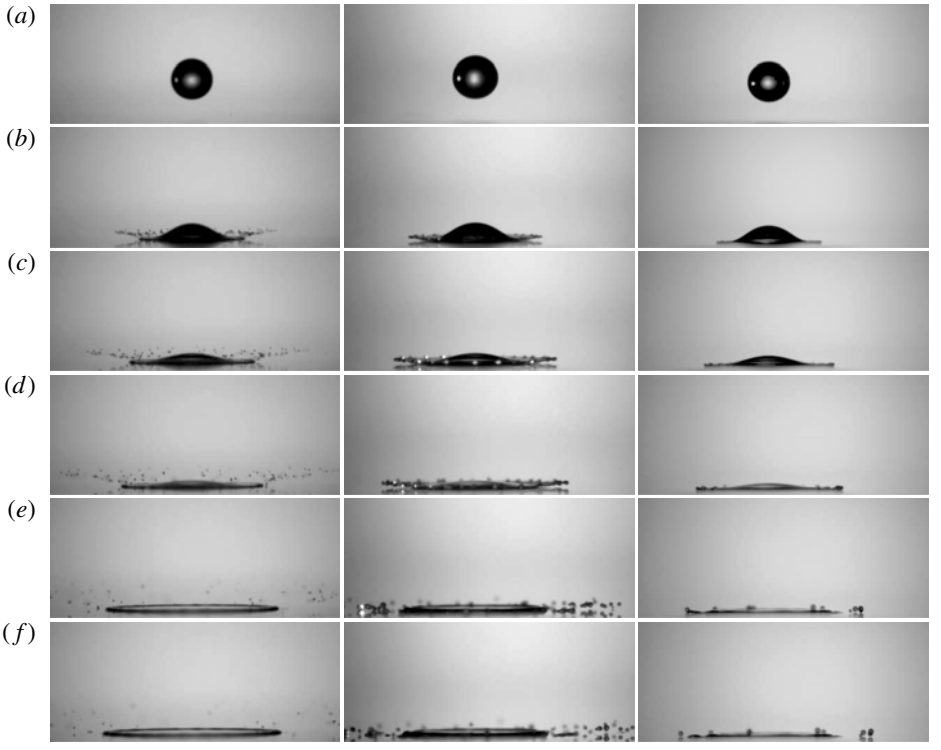

FIGURE 2. Effect of increasing viscosity on the splashing of a droplet for $V = 2.21 \pm 0.01$ m s^{-1} and $R = 0.88 \pm 0.023$ mm; from left to right, the viscosity μ is 1.3 cP (first column), 4.6 cP (second column) and 10.0 cP (third column). From top to bottom, each sequence of images corresponds to the instants when T is (*a*) -0.261 ms, (*b*) 0.609 ms, (*c*) 0.899 ms, (*d*) 1.189 ms, (*e*) 2.349 ms and (*f*) 2.929 ms. The temporal resolution is 58 μs.

$T \geqslant T_e$, where T_e is the ejection time in R&G and $T = 0$ is fixed at the instant when the drop first touches the substrate (see figure 1). When the impact speed is increased slightly (figure 1, second column), the lamella first dewets the substrate (figure 1*f*, second column) and then contacts it again (figure 1*g*, second column) as a consequence of the radial growth of the rim caused by capillary retraction. For velocities above the critical impact speed (image sequence in figure 1*a–k*, third column), the edge of the liquid sheet dewets the substrate and then breaks into droplets of characteristic radius R_d. These droplets are ejected outwards at a velocity substantially greater than that of the impact (figure 1*i–k*, third and fourth columns).

Figure 2 shows the effect of varying the liquid viscosity while keeping the impact velocity and the drop radius at nearly constant values. The three cases depicted correspond to impact velocities above the splash threshold, i.e. $V > V^*$. Figure 2 shows that an increase in liquid viscosity delays the instant at which droplets are first ejected and also decreases the small angle that the droplets form with the substrate, suggesting that the vertical velocity component of the droplets is far smaller than the radial component. Figures 1 and 2 also reveal that the fragmentation process starts from the ejection of small droplets which depart right from the rim bordering the radially expanding lamella. Thus, the disintegration of the edge of the liquid sheet

https://doi.org/10.1017/jfm.2015.223 Published online by Cambridge University Press

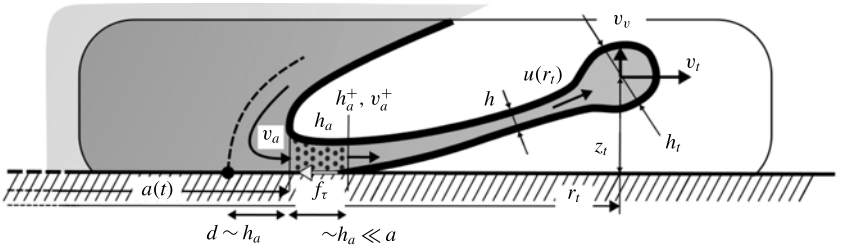

FIGURE 3. Sketch of the lamella for $T > T_e$ and for $V > V^*$, i.e. impact velocities above which the lamella dewets the substrate. This figure also illustrates the definitions of the different variables needed to describe the position of the rim and the region at the root of the lamella where the liquid is decelerated by viscosity. Note that since $a \propto t^{1/2}$ and $h_a \propto t^{3/2}$, $h_a \ll a$ for $t \ll 1$. The discontinuous line, located at a distance of $d \propto t^{3/2} \propto h_a$ from the jet root, limits the region from which fluid particles feed the lamella.

proceeds in a manner similar to that described by Villermaux & Bossa (2011) and Peters, van der Meer & Gordillo (2013).

3. Modelling the drop ejection process

The first steps in describing the disintegration of the drop that occurs during the initial period of time after impact are to determine the values of (i) the ejection time T_e, (ii) the initial tangential velocity of the edge of the lamella, $V_t(T_e)$, and (iii) its initial thickness, $H_t(T_e)$. For this purpose, we make use of some previous results from R&G; in that work, upon choosing R, V, R/V and ρV^2 as characteristic scales of length, velocity, time and pressure, respectively, with ρ being the liquid density and lowercase letters denoting dimensionless variables, the following properties are shown.

(i) The radius of the circular area shown in figures 1 and 3 evolves in time as $a = \sqrt{3t}$. For $T < T_e$, i.e. before the lamella is ejected, $a(t)$ represents the radius of the wetted area (figure 1). For $T > T_e$, a is the distance between the axis of symmetry of the drop and the radial position where the root of the lamella is located; therefore $a < r_t$, with r_t being the radial position of the rim (see figure 3).

(ii) The tangential velocity at which the lamella is initially ejected is $v_t(t_e) \simeq \dot{a}(t_e) = 1/2\sqrt{3/t_e}$.

(iii) The thickness of the edge of the lamella at the instant of ejection is $h_t \simeq \sqrt{12}\, t_e^{3/2}/\pi$.

(iv) Since $v_t = \dot{a}$ at $t = t_e$, i.e. the wetted area and the tip of the lamella advance at the same speed, and because the lamella can only be ejected if its tip advances faster than the radius of the wetted area, t_e is calculated from

$$c_1 Re^{-1} t_e^{-1/2} + Re^{-2} Oh^{-2} = \ddot{a} h_t^2 = c^2 t_e^{3/2}, \tag{3.1}$$

which expresses the fact that the ejection time is the instant at which the deceleration of the edge of the lamella coincides with the deceleration of the wetted area, $\ddot{a}$. In (3.1), $Re = \rho V R/\mu$ and $Oh = \mu/\sqrt{\rho R \sigma}$ denote, respectively, the impact Reynolds number and the Ohnesorge number (where σ is the interfacial tension coefficient), and $c_1 \simeq \sqrt{3}/2$ and $c^2 = 1.2$ are constants which are adjusted experimentally. In R&G it was also shown that the ejection time given by (3.1) has high-Oh and low-Oh limits $t_e = 2Re^{-1/2}$ and $t_e \propto Re^{-4/3} Oh^{-4/3}$, respectively.

https://doi.org/10.1017/jfm.2015.223 Published online by Cambridge University Press

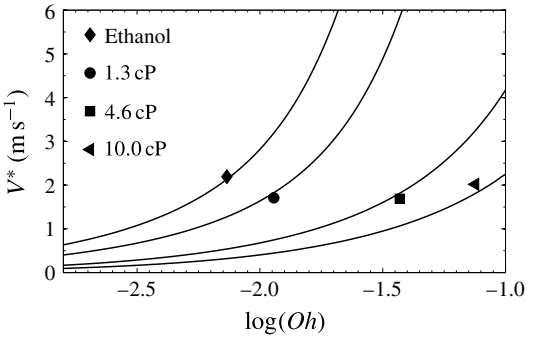

FIGURE 4. Experimental values of the critical impact velocity V^* for different values of the Ohnesorge number. The legend indicates the different fluids listed in table 1. Continuous lines represent results obtained from the model presented in R&G.

Moreover, in R&G it is shown that, once the sheet is ejected, its edge experiences a vertical lift force per unit length

$$\ell = K_l \mu_g V_t + K_u \rho_g V_t^2 H_t, \tag{3.2}$$

which results from the addition of the lubrication force exerted by the gas in the wedge region between the advancing lamella and the substrate, $K_l \mu_g V_t$, and the suction force exerted by the gas at the top part of the lamella, $K_u \rho_g V_t^2 H_t$. Here the subscript g represents gas quantities, $K_u \simeq 0.3$ is a constant determined numerically, and the expression

$$K_l \simeq -(6/\tan^2(\alpha)) \left[\ln(19.2\lambda/H_t) - \ln(1 + 19.2\lambda/H_t)\right], \tag{3.3}$$

where λ denotes the mean free path of gas molecules, is deduced using lubrication theory if one assumes that the front part of the lamella can be approximated by a wedge of constant angle $\alpha \sim 60^\circ$ while it is in contact with the substrate. Let us point out here that α refers to the angle that the advancing front forms with the substrate at the instant of ejection t_e (see R&G for details), so α is not related to the angle at which drops are ejected. Indeed, the ejected droplets form an angle with the substrate which can be approximated by the ratio between their vertical and horizontal velocity components.

Thus, the force balance projected in the vertical direction, $\rho H_t^2 \dot{V}_v \propto \ell$ with ℓ given by (3.2), provides the vertical velocity at which the lamella is initially expelled, namely,

$$V_v(T_e) = C_v \sqrt{\ell/(\rho H_t)}. \tag{3.4}$$

As shown in R&G, the good agreement of the model with their own experimental data as well as with the data of Mundo *et al.* (1995), Xu *et al.* (2005), Palacios *et al.* (2013) and Stevens (2014) indicates that the critical impact velocity V^*, above which the drop disintegrates into droplets, results from the condition that the vertical velocity (3.4) is such that $V_v/V_r \sim O(1)$, where $V_r = \sqrt{2\sigma/\rho H_t}$ is the capillary retraction velocity (Taylor 1959; Culick 1960), resulting in $\sqrt{\ell/(2\sigma)} \simeq 0.14$. Figure 4, which compares the splash threshold velocity V^* predicted by $\sqrt{\ell/(2\sigma)} \simeq 0.14$ with ℓ given by (3.2) and that measured experimentally for each of the four fluids listed in table 1, gives further support to our results in R&G. From now on, we will focus on the description of the drop fragmentation process for values of the velocity ratio $V/V^* > 1$.

https://doi.org/10.1017/jfm.2015.223 Published online by Cambridge University Press

So far, the theory in R&G has been tested for impact velocities below or equal to the critical speed, so first it is necessary to check whether the theory is equally applicable to calculating the initial values of $V_v(T_e)$ and $V_t(T_e)$ for $V > V^*$. We will show below that there is very good agreement between experimental data and the theoretical values, and so the next step in determining the velocities and sizes of the fragments ejected from the rim is to describe the liquid flow within the lamella formed for $t > t_e$ and extending from $r = a(t)$ to $r = r_t > a$ (see figure 3).

In R&G it is shown that when viscous effects are neglected, the thickness of the lamella and the liquid velocity at $a = \sqrt{3t}$, i.e. at the radial position where the root of the lamella is located, are given by

$$h_a = \frac{\sqrt{12}}{3\pi} t^{3/2} \quad \text{and} \quad v_a = \sqrt{3/t}, \tag{3.5a,b}$$

respectively, with these equations being valid for $a \lesssim 1$, i.e. $t \lesssim 1/3$. However, in a real fluid, a boundary layer of dimensional thickness $\Delta \sim \sqrt{\nu T_r} = \sqrt{\nu R/V}(h_a/v_a)^{1/2}$, where $T_r \sim R/Vh_a/v_a$ is the characteristic residence time of fluid particles entering the lamella, develops in the region $r \simeq \sqrt{3t}$. Indeed, from equation (6) in the supplementary data of R&G, it can be deduced that in the frame of reference moving at velocity $V\dot{a}$, there exists a stagnation point in the flow at dimensionless distance d from the root of the lamella, such that $\sqrt{a}\, d^{-1/2} \sim \dot{a} \Rightarrow d \propto t^{3/2} \propto h_a \ll \sqrt{3t}$ (see figures 1 and 3). Note that Δ is the width of a boundary layer that develops in a region of dimensionless width similar to the only relevant length scale characterizing this spatial region, namely the height of the root of the lamella. The effect of the viscous shear force per unit length exerted in this region, i.e. $F_\tau = \rho V^2 R f_\tau \sim \mu VR/\Delta v_a h_a$, is to decrease the liquid velocity from v_a to v_a^+ (see figure 3) and to increase the height of the lamella from h_a to h_a^+, with the expressions for v_a and h_a given in (3.5). To relate the downstream quantities v_a^+ and h_a^+ to their corresponding upstream values, we make use of integral balances of mass and momentum applied to the shaded region of figure 3, yielding $h_a v_a = h_a^+ v_a^+$ and $h_a v_a^2 - f_\tau = h_a^+ (v_a^+)^2$. Therefore, the equations

$$v_a^+ = v_a \left(1 - \sqrt{2}/\sqrt{Re\, v_a h_a}\right), \quad h_a^+ = h_a \left(1 - \sqrt{2}/\sqrt{Re\, v_a h_a}\right)^{-1}, \tag{3.6a,b}$$

constitute the initial conditions to be used next to predict the spatiotemporal evolution of the lamella; here $\sqrt{2}$ is a fixed proportionality constant and v_a and h_a are as given in (3.5). In (3.6), the viscous deceleration term is of order $\sim O(0.1)$ for the liquid with the smallest viscosity and ~ 0.5 for the liquid with $\mu = 10$ cP.

To describe the dynamics of the portion of the liquid sheet that extends from $r \simeq a(t)$ up to the radial position where the rim is located, i.e. $r = r_t$, we make use of the fact that the viscous shear stresses can be neglected in this region because the liquid is no longer in contact with the substrate; see the sketch in figure 3 and the images in figure 1(*d,e*), third and last columns. Additionally, since the local Weber number $We = Re^2 Oh^2$ characterizing the flow within the sheet is such that $We(v_a^+)^2 h_a \gg 1$, the gradients of capillary pressure are negligible, and so the momentum equation within the lamella reduces to

$$\frac{\mathrm{D}u}{\mathrm{D}t} = 0, \tag{3.7}$$

with $u(r, t)$ denoting the liquid velocity inside the lamella and $\mathrm{D}/\mathrm{D}t \equiv \partial/\partial t + u\partial/\partial r$ the material derivative. Equation (3.7) states that fluid particles conserve their

https://doi.org/10.1017/jfm.2015.223 Published online by Cambridge University Press

velocities for $\sqrt{3t} \lesssim r < r_t(t)$, i.e. up to the radial position $r_t(t)$ where the rim is located. The equation for the thickness of the liquid sheet $h(r,\ t)$ in the region $\sqrt{3t} \lesssim r < r_t(t)$ is deduced by making use of the mass balance, yielding

$$\frac{\partial(rh)}{\partial t} + \frac{\partial(rhu)}{\partial r} = 0 \Rightarrow \frac{\mathrm{D}\ln(rh)}{\mathrm{D}t} = -\frac{\partial u}{\partial r}. \tag{3.8}$$

Equations (3.7) and (3.8), which represent the ballistic motion of fluid particles along the lamella, are solved subject to the initial conditions $u(r = \sqrt{3t},\ t) = v_a^+$ and $h(r = \sqrt{3t},\ t) = h_a^+$, with v_a^+ and h_a^+ given in (3.6). Notice that, since $h_a \ll \sqrt{3t}$, we impose the boundary condition at $r = a(t)$ and neglect the width of the region $\sim O(h_a)$ where the boundary layer develops. To find the solution of the system (3.7) and (3.8), we used a Lagrangian numerical method which is quite similar to that described in Gekle & Gordillo (2010).

The radial and vertical positions of the edge of the lamella, $r_t(t)$ and $z_t(t)$, as well as its thickness $h_t(t)$, are deduced by applying the integral balances of mass and momentum at the rim (Taylor 1959):

$$\left.\begin{aligned} &\frac{\pi}{4}\frac{\mathrm{d}h_t^2}{\mathrm{d}t} = [u(r_t) - v_t]h(r_t), \qquad \frac{\mathrm{d}r_t}{\mathrm{d}t} = v_t, \\ &\frac{\pi h_t^2}{4}\frac{\mathrm{d}v_t}{\mathrm{d}t} = [u(r_t) - v_t]^2 h(r_t) - 2We^{-1}. \end{aligned}\right\} \tag{3.9}$$

In (3.9), the geometry of the rim has been approximated by a torus of minor radius $h_t(t)/2$. Moreover, the smallness of the angle that the spray forms with the substrate suggests approximating the projection of the capillary force per unit length in the direction tangential to the wall by $\simeq 2\sigma$; as a consequence of the smallness of the ratio ρ_g/ρ, air drag is neglected with respect to the flux of momentum entering the lamella. The equations in (3.9) need to be complemented with the force balance in the vertical direction,

$$\frac{\pi h_t^2}{4}\frac{\mathrm{d}v_v}{\mathrm{d}t} = -2We^{-1}\frac{z_t}{r_t} + \frac{1}{2}\frac{\rho_g}{\rho}C_l v_t^2 h_t \quad \text{with} \quad \frac{\mathrm{d}z_t}{\mathrm{d}t} = v_v, \tag{3.10}$$

where the projection of the capillary force per unit length in the direction normal to the wall has been approximated by $\simeq 2\sigma z_t/r_t$ and the lift coefficient has been taken to be a constant, $C_l = 1$. We assume that the influx of vertical momentum into the rim is negligible and, to simplify the model as much as possible, we do not take into account the dependence of C_l either on the angle of incidence or on the Reynolds number, because our description does not keep track of the orientation of the tip of the lamella with respect to the surrounding atmosphere. Since, as will be shown below, the theory in R&G is valid also for describing the ejection of the lamella for impact velocities above the critical velocity, (3.9) and (3.10) are solved subject to the following initial conditions:

$$\left.\begin{aligned} &r_t = \sqrt{3t_e}, \quad z_t = 0, \quad h_t = \sqrt{12}\,t_e^{3/2}/\pi, \\ &v_t = 1/2\sqrt{3/t_e}, \quad v_v = 2\sqrt{\ell/(\rho H_t V^2)}, \end{aligned}\right\} \tag{3.11}$$

where t_e is calculated using (3.1) for $\mu < 10$ cP and $t_e = 2Re^{-1/2}$ for $\mu = 10$ cP.

The final step to complete our theory is to model the breakup time t_b, i.e. the time at which drops are ejected from the edge of the lamella. In Lhuissier & Villermaux

https://doi.org/10.1017/jfm.2015.223 Published online by Cambridge University Press

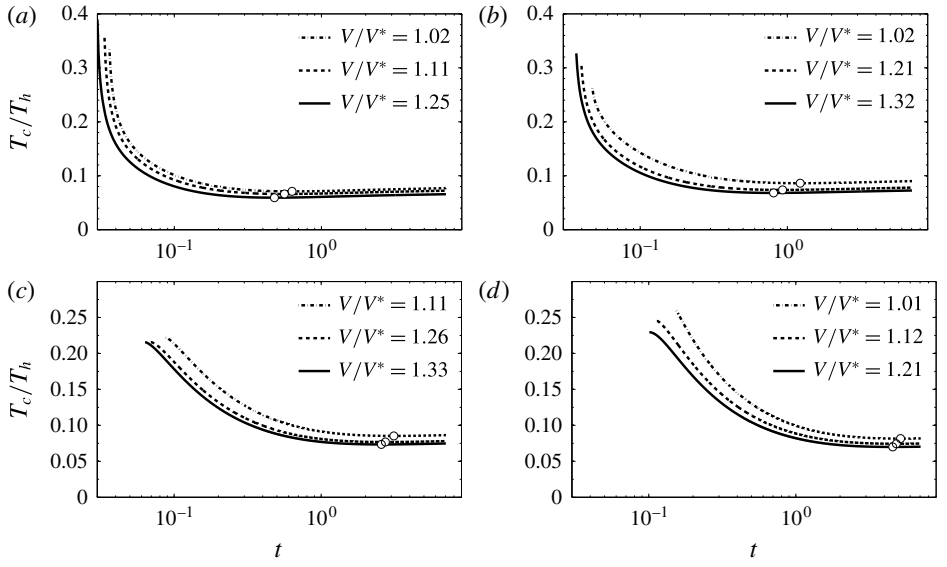

FIGURE 5. Calculated ratio $T_c/T_h = \sqrt{We/8}\,(h^{1/2})\,\mathrm{d}h/\mathrm{d}t$ for different impact velocities and the different liquids used in the experimental study: (*a*) ethanol, (*b*) decamethyltetrasiloxane, (*c*) poly(dimethylsiloxane) and (*d*) 10 cP silicone oil. The circles (○) indicate the instants $t_b = T_b V/R$ at which the model predicts the droplets will be ejected. Each of the curves starts at t_e.

(2011), Agbaglah, Josserand & Zaleski (2013), Peters *et al.* (2013) and references therein, it is clearly shown that the droplets making up the spray result from the amplification of Rayleigh–Taylor and capillary instabilities developing in the azimuthal direction (Thoroddsen *et al.* 2012). The growth rates of these instabilities, however, are highly attenuated as a consequence of simultaneous growth of the rim thickness. Thus, drops will only be ejected when the time characterizing the radial growth of the rim, $T_h = (1/H_t\,\mathrm{d}H_t/\mathrm{d}T)^{-1}$, is substantially greater than either the capillary time $T_c = (\rho H_t^3/8\sigma)^{1/2}$ or the viscous time $T_v = \mu H_t/\sigma$. In the present case, since the local Ohnesorge number is such that $T_v/T_c = \mu/\sqrt{\rho H_t \sigma} \ll 1$, the growth of perturbations will be controlled by the capillary rather than the viscous time. Figure 5 shows the time evolution of $T_c/T_h(t) = \sqrt{We/8}\,(h^{1/2})\,\mathrm{d}h/\mathrm{d}t$, calculated from (3.7)–(3.10) and solved subject to the initial conditions (3.6) and (3.11) for the different experimental conditions investigated. The function $T_c/T_h(t)$ reaches a constant value ~ 0.075 for times $T \approx T_b$, with T_b such that $(\mathrm{d}/\mathrm{d}T)[T_c/T_h](T = T_b) = 0$. In our model, we assume that drops are ejected precisely at t_b. This choice of t_b is justified by taking into account the following facts (Eggers & Villermaux 2008): (i) the characteristic time of growth of a capillary instability is $\sim 3T_c$; (ii) Rayleigh's stability analysis of capillary perturbations reveals that the dimensionless wavenumber k with fastest growth rate is $k = \pi H_t/\lambda \simeq 0.7$, where λ is the wavelength of the perturbation, which is kept constant in time; (iii) the growth of capillary instabilities is inhibited for $k \geqslant 1$. Therefore, in order for capillary corrugations with characteristic initial wavenumbers $k = 0.7$ to be amplified up to the point that drops are ejected from the rim, it is necessary that in time $3T_c$, the variation of the dimensionless wavenumber is such that $\Delta k < 0.3$. This condition is equivalent to $\mathrm{d}H_t/\mathrm{d}T \times 3T_c \lesssim 0.3H_t \Rightarrow T_c/T_h \lesssim 0.1$, a value that is very close to and slightly larger than the minimum value of T_c/T_h, which

https://doi.org/10.1017/jfm.2015.223 Published online by Cambridge University Press

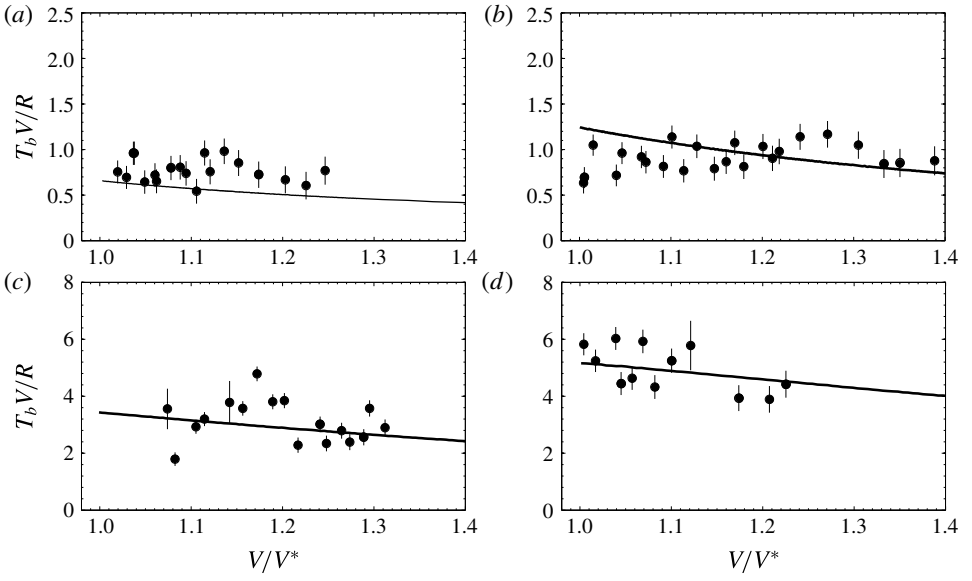

FIGURE 6. Comparison of the predicted breakup time t_b with the experimentally obtained value for (*a*) ethanol, (*b*) decamethyltetrasiloxane, (*c*) poly(dimethylsiloxane) and (*d*) 10 cP silicone oil.

is approximately 0.075. Note from figure 5 that our criterion for choosing the instant of drop ejection is consistent with the previous arguments. However, the way T_b is calculated is nothing but a plausible assumption: indeed, in a real experiment, the breakup time will depend strongly on the initial amplitude of azimuthal perturbations. In addition, the determination of T_b from very flat curves such as those in figure 5 may result in a non-negligible uncertainty in the determination of the breakup time.

Moreover, since $T_c \ll T_b$, drops will be ejected slightly after T_b is reached. Hence we neglect the contribution of T_c and assume that drops will be ejected right at T_b, with their velocities and sizes determined from the solution of (3.7)–(3.10) subject to the initial conditions (3.6) and (3.11) at the particular instant $t_b = T_bV/R$. Let us point out that, in our description, we assume that the mean diameters of the first drops ejected can be approximated by the thickness of the rim at $t = t_b$. The reason behind this approximation is the following: the volume of liquid contained in a rim of diameter $h(t_b)$ along a distance in the azimuthal direction equivalent to that of the most unstable capillary wavelength ($\simeq 4.5h(t_b)$) would give rise to the ejection of a droplet with diameter $\simeq 1.9h_t(t_b)$. However, only a fraction of this volume will be ejected as a droplet; in fact, the simulations in Agbaglah *et al.* (2013) and the experiments of Thoroddsen *et al.* (2012) show that the diameters of the drops ejected are quite similar to the diameter of the rim, and this is the reason that in our model we identify the diameters of the drops with that of the rim at $t = t_b$.

Figure 6, which compares the measured ejection time with the value of t_b calculated as $(\mathrm{d}/\mathrm{d}t)[h^{1/2}\,\mathrm{d}h/\mathrm{d}t]\,(t = t_b) = 0$ (where t_b is the value marked with a circle in figure 5) for each of the four fluids investigated and for different impact velocities, validates our approach.

https://doi.org/10.1017/jfm.2015.223 Published online by Cambridge University Press

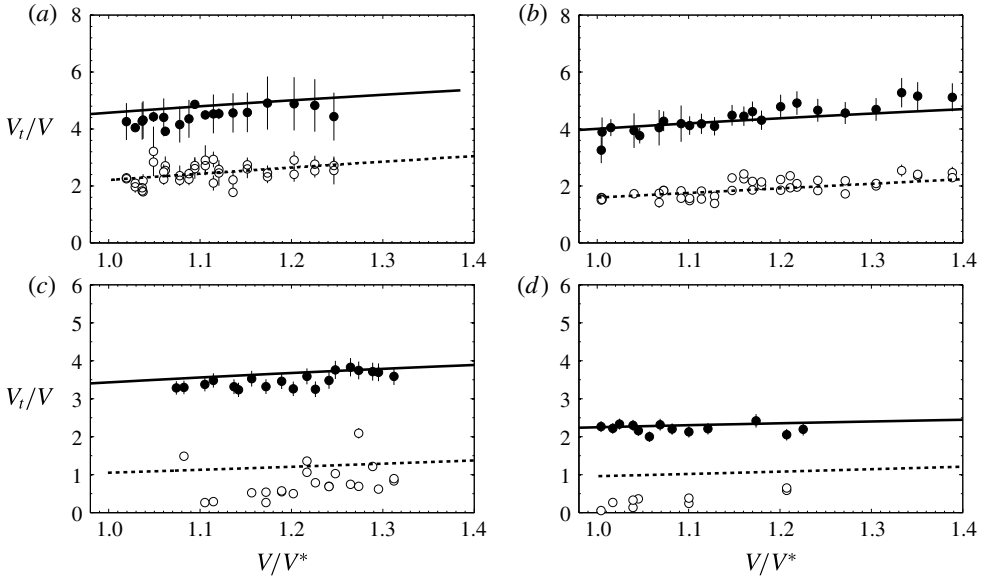

FIGURE 7. Tangential velocity of the lamella for impact velocities greater than the critical velocity V^*, at the ejection time $t = t_e$ (●) and at the breakup instant $t = t_b$ (○), for (*a*) ethanol, (*b*) decamethyltetrasiloxane, (*c*) poly(dimethylsiloxane) and (*d*) 10 cP silicone oil; the lines represent results obtained from the model.

4. Comparison between observations and the model

Figures 7 and 8 show the horizontal (v_t) and vertical (v_v) velocity components of the tip of the lamella at the instant of ejection t_e and at the breakup time t_b, for each of the four fluids investigated. The tangential and vertical velocities at t_e are calculated, respectively, from $v_t(t_e) = \dot{a}(t_e) = 1/2\sqrt{3/t_e}$ and (3.4), with $C_v = 2$ and t_e determined either using (3.1) for $\mu < 10$ cP or by means of the high-Oh limit $t_e = 2Re^{-1/2}$ for $\mu = 10$ cP. The results shown in figures 7 and 8 indicate that the theoretical description of the ejection of the lamella in R&G can indeed be extended to describe the drop fragmentation process for impact velocities above the critical velocity, i.e. for $V > V^*$. Moreover, observe that for a given fluid, $v_t(t_e) \gg v_v(t_e)$, which implies that the trajectory of the edge of the lamella forms a small angle with the substrate, in accordance with the experimental evidence shown in figures 1 and 2. This observation is more evident in figures 9 and 10, where the measured radial (r_t) and vertical (z_t) positions of the edge of the lamella are compared with our model predictions. Note that the agreement is remarkable for all four types of fluid investigated and also, as anticipated above, $z_t \ll r_t$. Furthermore, the trajectories of the tip of the lamella in figures 9 and 10, represented up to $t = 0.4 > 1/3$, are calculated consistently with the range of validity of (3.5). Indeed, figure 11 shows that the fluid particles entering the rim at the instant t were ejected from the root of the jet at $t_a < 1/3$.

Figures 7 and 8 also reveal that, while $v_t(t_e)$ increases slightly with V/V^*, $v_v(t_e)$ remains practically unchanged within the range of impact velocities investigated. Also, observe from figures 7 and 8 that both $v_t(t_e)$ and $v_v(t_e)$ decrease when the liquid viscosity is increased. Observe that all the experimental measurements at t_e are captured by our theory, not only qualitatively but also quantitatively.

https://doi.org/10.1017/jfm.2015.223 Published online by Cambridge University Press

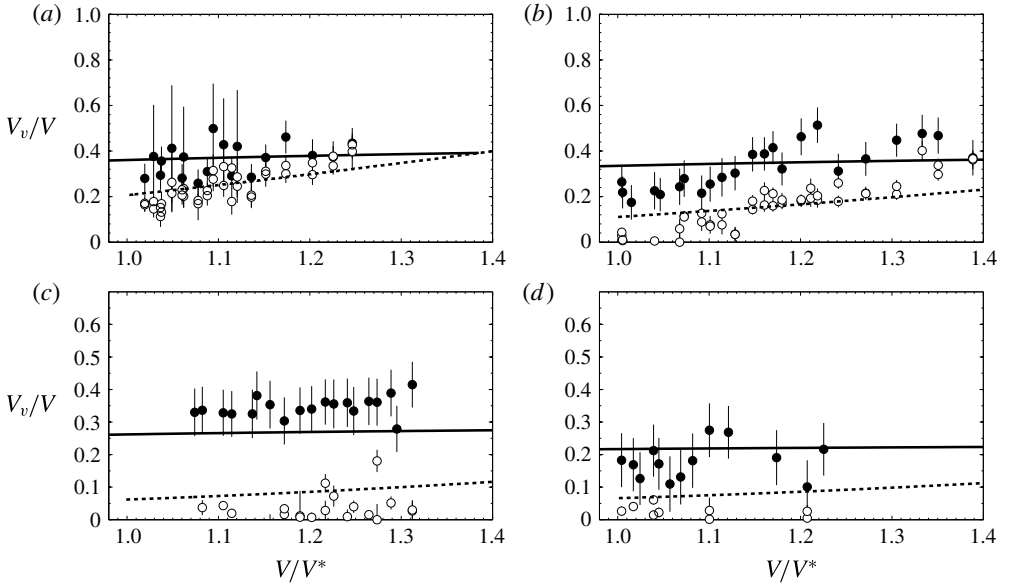

FIGURE 8. Vertical velocity of the lamella for impact velocities greater than the critical velocity V^*, at the ejection time $t = t_e$ (●) and at the breakup instant $t = t_b$ (○), for (*a*) ethanol, (*b*) decamethyltetrasiloxane, (*c*) poly(dimethylsiloxane) and (*d*) 10 cP silicone oil; the lines represent results obtained from the model.

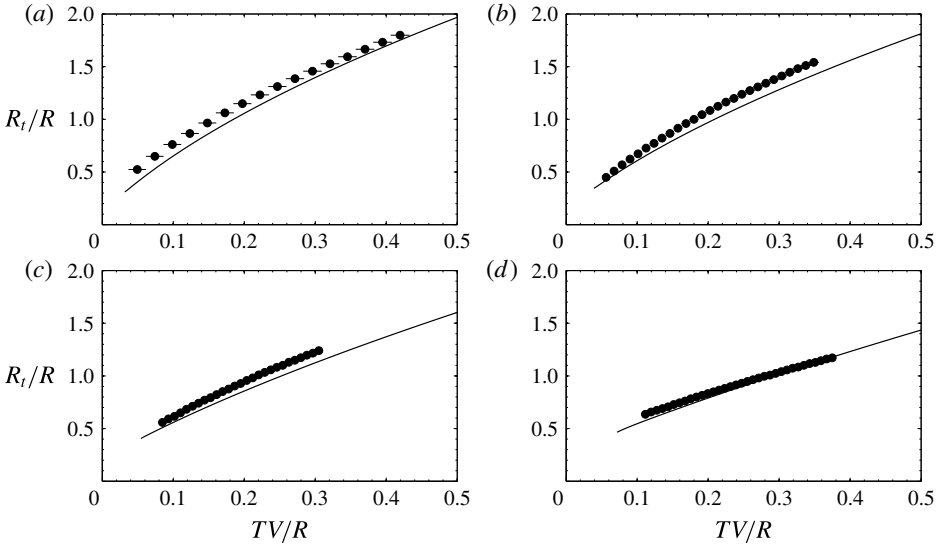

FIGURE 9. Horizontal position of the edge of the lamella plotted as a function of time. The panels correspond to the different fluids listed in table 1: (*a*) ethanol, with $V/V^* = 1.15$; (*b*) decamethyltetrasiloxane, with $V/V^* = 1.20$, (*c*) poly(dimethylsiloxane), with $V/V^* = 1.24$; (*d*) 10 cP silicone oil, with $V/V^* = 1.00$. Continuous lines represent results obtained from the model.

https://doi.org/10.1017/jfm.2015.223 Published online by Cambridge University Press

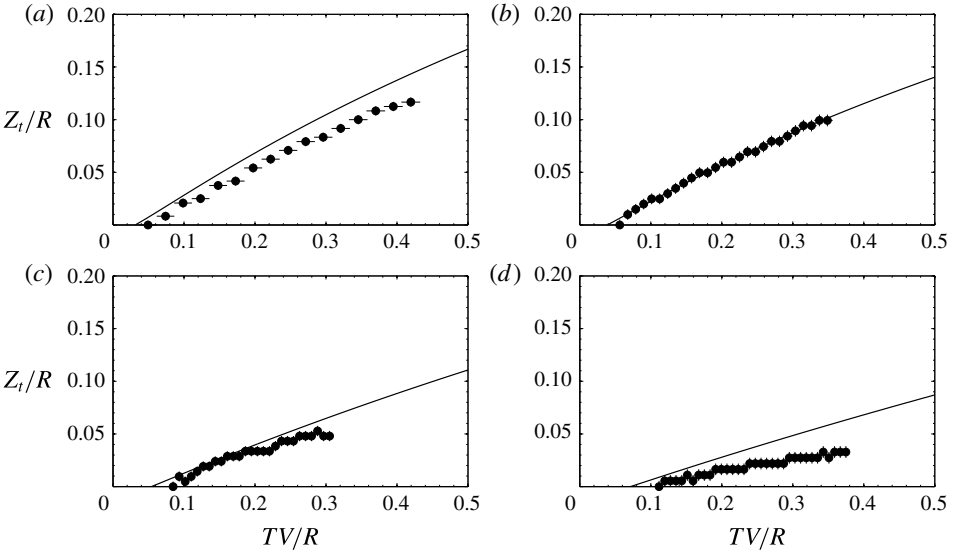

FIGURE 10. Vertical position of the edge of the lamella plotted as a function of time. The panels correspond to the different fluids listed in table 1: (*a*) ethanol, with $V/V^* = 1.15$; (*b*) decamethyltetrasiloxane, with $V/V^* = 1.20$, (*c*) poly(dimethylsiloxane), with $V/V^* = 1.24$; (*d*) 10 cP silicone oil, with $V/V^* = 1.00$. Continuous lines represent results obtained from the model.

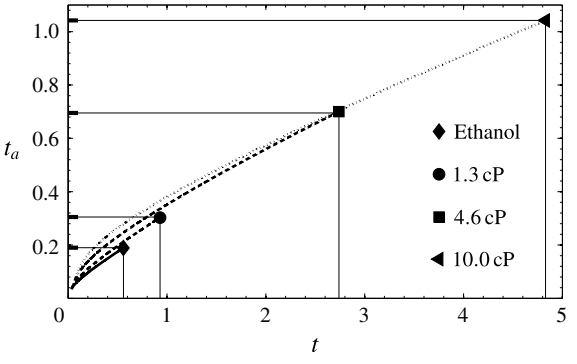

FIGURE 11. Plotted along the vertical axis, t_a is the instant at which a fluid particle entering the rim at instant t was ejected from the root of the lamella. The symbols indicate the breakup times $t = t_b$ for the following cases: (◆) ethanol, with $V/V^* = 1.11$; (●) decamethyltetrasiloxane, with $V/V^* = 1.21$; (■) poly(dimethylsiloxane), with $V/V^* = 1.26$; (◀) 10 cP silicone oil, with $V/V^* = 1.12$.

The main purpose of our model, however, is to predict the horizontal and vertical velocity components as well as the diameters of the droplets formed at the edge of the lamella. Figures 7 and 8 show that, as a consequence of the capillary deceleration of the rim, $v_t(t_e) > v_t(t_b)$ and $v_v(t_e) > v_v(t_b)$, with the velocities at t_b calculated by solving the system (3.7)–(3.10) subject to the initial conditions predicted by our theory, i.e. (3.6) and (3.11). The agreement between our theory and the experimental

https://doi.org/10.1017/jfm.2015.223 Published online by Cambridge University Press

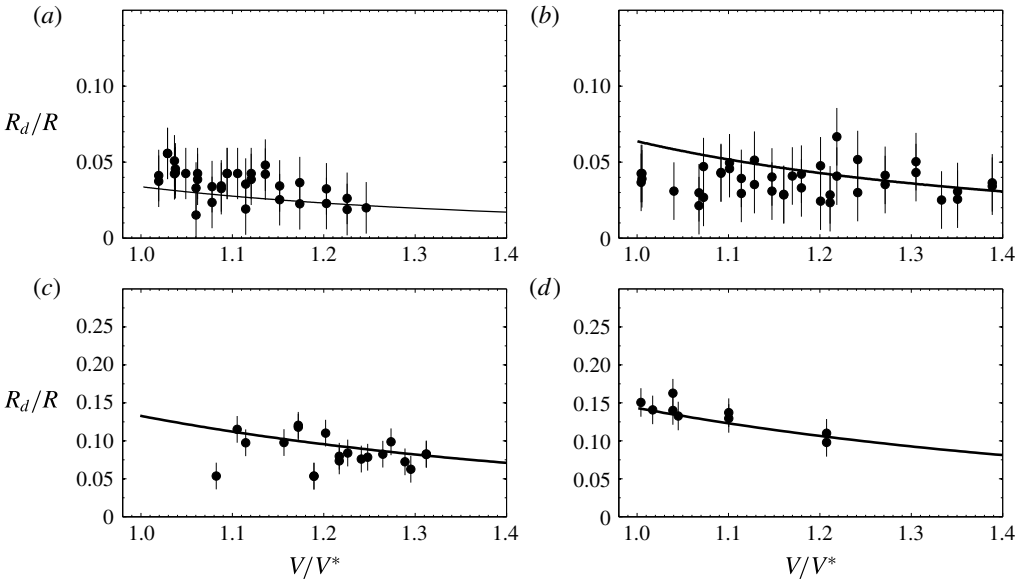

FIGURE 12. Comparison of the predicted radius of the first droplets ejected with experimentally measured values for (*a*) ethanol, (*b*) decamethyltetrasiloxane, (*c*) poly(dimethylsiloxane) and (*d*) 10 cP silicone oil.

measurements is quantitative for all the fluids listed in table 1, except for the liquid with the largest viscosity.

The reason for the discrepancies observed with the liquid of $\mu = 10$ cP is probably related to the fact that the breakup time in this case is so large that $t_a > 1/3$, exceeding the limit of validity of (3.5) (see figure 11). Therefore, for $t_a > 1/3$, the equations in (3.5) should be replaced, for instance, by analogous expressions such as those in Eggers *et al.* (2010). This step is beyond the scope of the present study, which, as shown above, captures very well the sizes and velocities of the drops ejected in the cases of low-viscosity liquids.

In spite of the fact that the model is unable to accurately predict the velocities of the fragments ejected for $\mu = 10$ cP, it is noteworthy that our approach gives good quantitative predictions of the sizes of the first drops ejected from the rim, as figure 12 shows. Finally, as a further test of our theory, in figure 16 of appendix B we compare the predictions of our model with the experimental results of Thoroddsen *et al.* (2012), who studied the velocities and sizes of fragments ejected after the impact of high-speed water droplets; good agreement is obtained. The evidence in appendix B indicates that the model presented here is useful not only for quantifying the ejection of the fastest fragments generated after drop splashing at t_b, but also in describing the continuous drop disintegration process that takes place for larger times.

5. Concluding remarks

In this paper we have presented a model for predicting the sizes and velocities of fragments ejected after a drop impacts a smooth wall at a velocity above the critical speed described in Riboux & Gordillo (2014), extending and providing further support for our theory in R&G. The present description can be summarized as follows.

https://doi.org/10.1017/jfm.2015.223 Published online by Cambridge University Press

Fluid particles conserve the tangential velocity V_a^+ given in (3.6) that they possessed downstream of a narrow region of typical length $\sim H_a$ located where the drop meets the substrate, $\simeq\sqrt{3RVT}$. Downstream of the region of length $\sim H_a$ in which the fluid is decelerated by viscous friction, the sheet is no longer in contact with the substrate, and therefore the radial velocities of fluid particles are conserved up to the radial position where the rim is located. The rim itself is accelerated radially outwards as a consequence of the influx of momentum transported by fluid particles ejected from the location $\simeq\sqrt{3RVT}$, and is decelerated due to the action of the capillary forces. The rim, of initial thickness $H_t(T_e) \ll R$, also translates in the direction perpendicular to the wall, thanks to the initial vertical velocity imparted by the lift force per unit length, ℓ, given in (3.2), as well as by the lift force $1/2\rho_g V_t^2 H_t C_l$; capillarity contributes to decelerate the rim vertically. Finally, droplets are ejected because the development of capillary and Rayleigh–Taylor instabilities favours the generation of corrugations of increasing amplitude, which give rise to the formation and ejection of drops at the instant when the ratio T_h/T_c becomes large enough. Here we have characterized this instant T_b as the time at which T_c/T_h reaches a minimum, with $T_c/T_h \simeq 0.075$. Here T_h and T_c denote the characteristic times of growth of the rim thickness and of capillary instabilities, respectively. The diameters of the drops are close to the diameter of the rim at T_b, and their velocities are approximately equal to the rim velocity at this instant.

Let us point out here that these results are valid for the case of smooth and partially wetting solids with a static contact angle of $\sim 20°$. We would like to extend the theory in R&G to a wider range of static contact angles and also to rough surfaces.

Acknowledgements

This work was supported by the Spanish MINECO under Project DPI2011-28356-C03-01, partly financed through European funds.

Appendix A. Detection of the ejected droplets

The axisymmetry of the drop ejection process, which is recorded in a focus plane perpendicular to the solid substrate, suggests that we divide each of the images making up the experimental video sequence into two symmetrical parts with respect to the line perpendicular to the point where the drop first touches the substrate, $X = 0$ (see figure 13). The image processing algorithm developed here follows over time the positions of the fastest droplets ejected from each of the sides ($X \lessgtr 0$) and also provides their equivalent radii. To do so, the algorithm first computes the time evolution of the variance of the grey intensity at each of the vertical lines making up the Eulerian meshgrid depicted in figure 13. Due to the fact that the disintegration process does not take place in a preferential azimuthal direction, the analysis of the experimental information obtained at the focus plane is enough to describe the full drop ejection process. Figure 14(*a*) reveals that there exists an instant, marked with a circle, at which the variance of the grey intensity of each of the vertical lines experiences an abrupt change. Since this is precisely the instant at which the fastest drop reaches a fixed horizontal distance from the impact point, the slope of the line depicted in figure 14(*b*) (in pixels s^{-1}) is proportional to the horizontal velocity of the first drop ejected in the focus plane. This velocity is used to estimate the horizontal position of the first ejected drop, and this information is used to define a box that encloses the drop and moves with the predicted horizontal velocity. The position

https://doi.org/10.1017/jfm.2015.223 Published online by Cambridge University Press

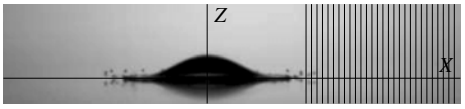

FIGURE 13. Image showing the vertical grid lines used to predict the velocity of the first ejected droplets.

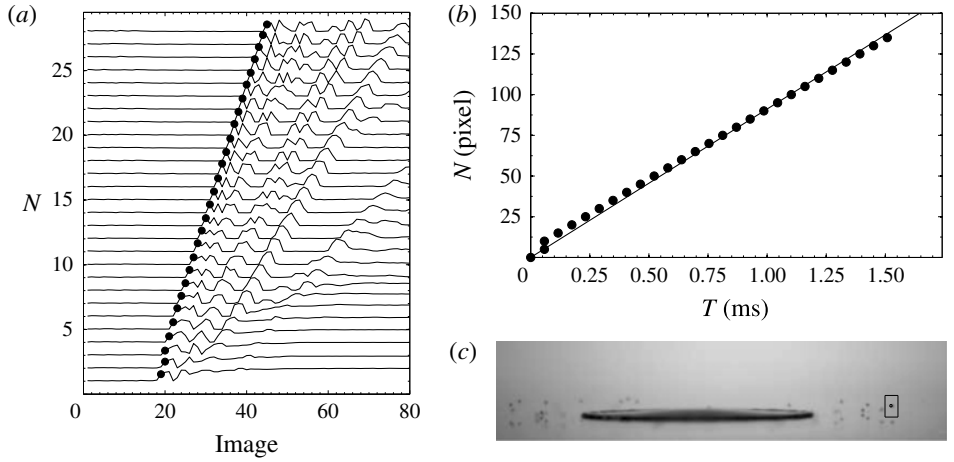

FIGURE 14. (*a*) Evolution of the variance of the grey intensity as a function of the image sequence for each of the vertical lines used in the predictor step; the black marker point indicates the instant at which the fastest droplet crosses a given vertical line. (*b*) Horizontal position of the black marker point in (*a*) as a function of time. (*c*) Detection of the droplet position and the droplet area by means of a box moving at the predicted horizontal velocity.

$(X_d,\ Z_d)$ of the barycentre of the drop and its area A are obtained using the image processing toolbox of Matlab. The horizontal and vertical velocity components of the first ejected drop are then accurately calculated as $V_t = \mathrm{d}X_d/\mathrm{d}T$ and $V_v = \mathrm{d}Z_d/\mathrm{d}T$, whereas the equivalent radius is $R_d = \sqrt{A/\pi}$, as shown in figure 15.

Appendix B. Comparison of the model predictions with the experimental results of Thoroddsen *et al.* (2012)

The limitations in spatiotemporal resolution of our experimental set-up prevented us from studying the details of the disintegration of splashing water droplets. Consequently, our experimental study does not cover a significant variation of the interfacial tension coefficient. Therefore, to further validate our model, we make use of the experimental data from Thoroddsen *et al.* (2012), where the velocities of the fragments ejected after the splashing of a water droplet of diameter ∼5.5 mm impacting on a smooth substrate at velocity $V \simeq 5$ m s^{-1} are represented as a function of both the drop size and the time after impact. The high impact speed of the drops analysed in Thoroddsen *et al.* (2012) inhibits the formation of a long lamella; in fact, the fragments are ejected slightly downstream of the root of the jet, i.e. drops are ejected from $r_t \simeq a(t)$. Therefore, in order to make comparisons with these experimental results, in figure 16(*a*) we represent the values of Vv_a^+ as a function of

https://doi.org/10.1017/jfm.2015.223 Published online by Cambridge University Press

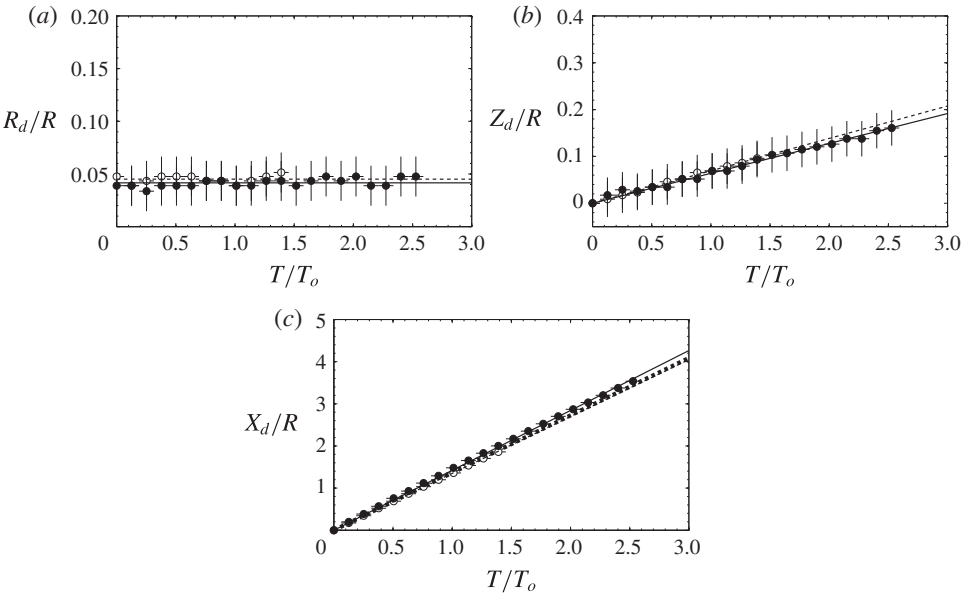

FIGURE 15. Plots of (*a*) droplet equivalent radius, (*b*) vertical velocity component and (*c*) horizontal velocity component of the fastest droplets ejected in the regions $X > 0$ (○) and $X < 0$ (●). The thick dashed line in (*c*) represents the horizontal velocity calculated in the predictor detection process; see figure 14(*b*).

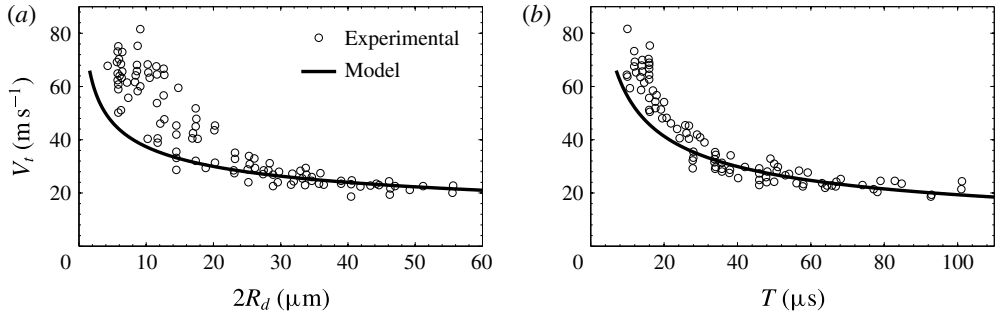

FIGURE 16. (*a*) Comparison of the experimental velocity of the ejected droplets as a function of their diameter (from figure 5a of Thoroddsen *et al.* 2012) with the predicted velocity of the fragments, Vv_a^+, as a function of $Rh_a^+ \simeq 2R_d$, where v_a^+ and h_a^+ are given in (3.5) and (3.6). (*b*) Comparison of the velocity of the ejected fragments as a function of the time after impact (from figure 5b of Thoroddsen *et al.* 2012) with the predicted velocity Vv_a^+ given in (3.6). The fluid used by Thoroddsen *et al.* (2012) is water, and the Reynolds number based on the drop radius is $Re \approx 1.45 \times 10^4$. The ejection time calculated from (3.1) using the experimental parameters in Thoroddsen *et al.* (2012) is $T_e \simeq 7$ μs, in agreement with the experimental observations.

Rh_a^+, and in figure 16(*b*) we plot Vv_a^+ as a function of the time after impact, where v_a^+ and h_a^+ are calculated from (3.5) and (3.6) for times $t \geqslant t_e$, with t_e given by (3.1). Figure 16 shows that our model is able to faithfully capture the ejection time as well as the velocities and sizes of the ejected drops for times slightly above t_e. Indeed,

https://doi.org/10.1017/jfm.2015.223 Published online by Cambridge University Press

note that the fragmentation process for times closer to t_e is affected by the oscillation phase of the impacting droplets, which are deformed away from the spherical shape by air resistance Thoroddsen *et al.* (2012), a fact which explains the slight deviation of the prediction for times below 15 μs. Moreover, in Thoroddsen *et al.* (2012), with values of the Reynolds and Weber numbers based on R, namely $Re = 9900$ and $We = 490$, the ejection time for impacting droplets was reported to be $T_e \sim 10$ μs, a value that has an associated uncertainty of $\simeq 1$ μs, since the acquisition frequency is 5×10^5 f.p.s. The value of the ejection time calculated using (3.1) is $T_e \simeq 12$ μs. All of this evidence suggests that the model presented here is useful not only for quantifying the ejection of the fastest fragments generated after drop splashing at t_b, but also in describing the continuous drop disintegration process taking place for larger times.

REFERENCES

AGBAGLAH, G., JOSSERAND, C. & ZALESKI, S. 2013 Longitudinal instability of a liquid rim. *Phys. Fluids* **25**, 022103.

BIRD, J. C., DHIMAN, R., KWON, H.-M. & VARANASI, K. K. 2013 Reducing the contact time of a bouncing drop. *Nature* **503**, 385–388.

BIRD, J. C., TSAI, S. S. H. & STONE, H. A. 2009 Inclined to splash: triggering and inhibiting a splash with tangential velocity. *New J. Phys.* **11**, 063017.

CULICK, F. E. C. 1960 Comments on a ruptured soap film. *J. Appl. Phys.* **31**, 1128–1129.

DRISCOLL, M. M., STEVENS, C. S. & NAGEL, S. R. 2010 Thin film formation during splashing of viscous liquids. *Phys. Rev.* E **82**, 036302.

DUCHEMIN, L. & JOSSERAND, C. 2011 Curvature singularity and film-skating during drop impact. *Phys. Fluids* **23**, 091701.

DUEZ, C., YBERT, C., CLANET, C. & BOCQUET, L. 2007 Making a splash with water repellency. *Nat. Phys.* **3**, 180–183.

EGGERS, J., FONTELOS, M. A., JOSSERAND, C. & ZALESKI, S. 2010 Drop dynamics after impact on a solid wall: theory and simulations. *Phys. Fluids* **22**, 062101.

EGGERS, J. & VILLERMAUX, E. 2008 Physics of liquid jets. *Rep. Prog. Phys.* **71** (3), 036601.

GEKLE, S. & GORDILLO, J. M. 2010 Generation and breakup of Worthington jets after cavity collapse. Part 1. Jet formation. *J. Fluid Mech.* **663**, 293–330.

JOSSERAND, C. & ZALESKI, S. 2003 Droplet splashing on a thin liquid film. *Phys. Fluids* **15**, 1650–1657.

KOLINSKI, J. M., RUBINSTEIN, S. M., MANDRE, S., BRENNER, M. P., WEITZ, D. A. & MAHADEVAN, L. 2012 Skating on a film of air: drops impacting on a surface. *Phys. Rev. Lett.* **108**, 074503.

LATKA, A., STRANDBURG-PESHKIN, A., DRISCOLL, M. M., STEVENS, C. S. & NAGEL, S. R. 2012 Creation of prompt and thin-sheet splashing by varying surface roughness or increasing air pressure. *Phys. Rev. Lett.* **109**, 054501.

LHUISSIER, H. & VILLERMAUX, E. 2011 The destabilization of an initially thick liquid sheet edge. *Phys. Fluids* **23**, 091705.

MANDRE, S., MANI, M. & BRENNER, M. P. 2009 Precursors to splashing of liquid droplets on a solid surface. *Phys. Rev. Lett.* **102**, 134502.

MUNDO, C., SOMMERFELD, M. & TROPEA, C. 1995 Droplet-wall collisions: experimental studies of the deformation and breakup process. *Intl J. Multiphase Flow* **21**, 151–173.

PALACIOS, J., HERNANDEZ, J., GOMEZ, P., ZANZI, C. & LOPEZ, J. 2013 Experimental study of splashing patterns and the splashing/deposition threshold in drop impacts onto dry smooth solid surfaces. *Exp. Therm. Fluid Sci.* **44**, 571–582.

PETERS, I. R., VAN DER MEER, D. & GORDILLO, J. M. 2013 Splash wave and crown breakup after disc impact on a liquid surface. *J. Fluid Mech.* **724**, 553–580.

https://doi.org/10.1017/jfm.2015.223 Published online by Cambridge University Press

RIBOUX, G. & GORDILLO, J. M. 2014 Experiments of drops impacting a smooth solid surface: a model of a critical impact speed for drop splashing. *Phys. Rev. Lett.* **113**, 024507.

RICHARD, D., CLANET, C. & QUERE, D. 2002 Contact time of a bouncing drop. *Nature* **417**, 811–811.

RIOBOO, R., MARENGO, M. & TROPEA, C. 2002 Time evolution of liquid drop impact onto solid, dry surfaces. *Exp. Fluids* **33**, 112–124.

STEVENS, C. S. 2014 Scaling of the splash threshold for low-viscosity fluids. *Europhys. Lett.* **106**, 24001.

TAYLOR, G. I. 1959 The dynamics of thin sheets of fluid. II. Waves on fluid sheets. *Proc. R. Soc. Lond.* A **253** (1274), 296–312.

THORODDSEN, S. T., TAKEHARA, K. & ETOH, T. G. 2012 Micro-splashing by drop impacts. *J. Fluid Mech.* **706**, 560–570.

VILLERMAUX, E. & BOSSA, B. 2011 Drop fragmentation on impact. *J. Fluid Mech.* **668**, 412–435.

WORTHINGTON, A. M. 1908 *A Study of Splashes*. Longman and Green.

XU, L., ZHANG, W. W. & NAGEL, S. R. 2005 Drop splashing on a dry smooth surface. *Phys. Rev. Lett.* **94**, 184505.

YARIN, A. L. 2006 Drop impact dynamics: splashing, spreading, receding, bouncing. *Annu. Rev. Fluid Mech.* **38**, 159–192.

https://doi.org/10.1017/jfm.2015.223 Published online by Cambridge University Press